Materials Today Advances 9 (2021) 100135

Contents lists available at ScienceDirect

Materials Today Advances

journal homepage: www.journals.elsevier.com/materials-today-advances/

Conductive and highly compressible MXene aerogels with ordered microstructures as high-capacity electrodes for Li-ion capacitors

J. Orangi [a], H. Tetik [b], P. Parandoush [b], E. Kayali [a], D. Lin [b, *], M. Beidaghi [a, **]

[a] Department of Mechanical and Materials Engineering, Auburn University, Auburn, Al, 36849, USA
[b] Department of Industrial and Manufacturing Systems Engineering, Kansas State University, Manhattan, KS, 66506, USA

ARTICLE INFO

Article history:
Received 15 October 2020
Received in revised form
8 December 2020
Accepted 22 December 2020
Available online 13 February 2021

Keywords:
2D MXenes
Unidirectional freeze casting
Highly compressible materials
Vertically aligned microstructure
Electrochemical energy storage

ABSTRACT

Assembling two-dimensional (2D) materials into functional three-dimensional (3D) structures can enable their use in a wide variety of applications. For energy storage devices, 3D electrodes with high ionic and electronic transport properties and decent mechanical properties are expected to prompt the fabrication of the next generations of devices with high energy and power densities. Herein, we report a simple, efficient, and scalable process based on unidirectional freeze casting to fabricate ordered and porous 3D aerogels from 2D $Ti_3C_2T_x$ MXene flakes. The fabricated aerogels show excellent mechanical, electrical, and electrochemical properties. Our studies show that the processing conditions significantly affect the properties of MXene aerogels. The electrical conductivity and mechanical properties of fabricated aerogels directly correlate with their structural features. The mechanical test results showed that MXene aerogels with ordered structures could withstand almost 50% of strain before recovering to their original shape and maintain their electrical conductivities during continuous compressive cycling. As electrode materials for lithium-ion capacitors, the fabricated aerogels delivered a significantly high specific capacity (~1210 mAh/g at 0.05 A/g), excellent rate capability (~200 mAh/g at 10 A/g), and outstanding cycling performance. We believe that the MXene aerogels with ordered structures have promising properties for a broad range of applications, including energy storage devices and strain sensors.

1. Introduction

Assembling two-dimensional (2D) materials into functional three-dimensional (3D) structures can enable applications of these materials in various fields. 3D aerogels, hydrogels, and foams fabricated by the assembly of 2D materials show interesting physical properties, such as high specific surface areas, high porosities, low densities, and interconnected conductive networks [1–3]. Therefore, materials with 3D structures, such as aerogels, have shown promising performances for a range of applications, including catalysis [4], stretchable electronics [5,6], supercapacitors [7–9], hydrogen storage [10], and environmental protection [11]. However, further implementation of aerogels based on 2D materials for functional applications is dependent on addressing various challenges specific to each application. For energy storage applications, such as electrodes of batteries and electrochemical capacitors, one of the main challenges is engineering the structure of aerogels to enhance their ionic and electronic transport and mechanical properties to meet practical usage requirements. Another critical challenge is the fabrication of aerogels using materials with intrinsically higher electronic conductivities and electrochemical performances.

In the past few years, much research has been dedicated to improving the properties of electrodes used in batteries and supercapacitors by understanding their structure–property relationships [12,13]. For aerogel electrodes based on 2D materials, controlling the porosity and the density of the electrodes to improve ionic and electronic properties has been a major theme of research as these properties can be readily controlled by changing processing conditions [14]. Further improvement of these properties can be achieved by controlling the orientation and the interconnected network of 2D sheets in the structure of aerogels, which is significantly more challenging. Herein, we report a general strategy based on unidirectional freeze casting to fabricate 3D

* Corresponding author.
** Corresponding author.
E-mail addresses: dongl@ksu.edu (D. Lin), mbeidaghi@auburn.edu (M. Beidaghi).

https://doi.org/10.1016/j.mtadv.2021.100135

freestanding MXene aerogels with excellent mechanical, electrical, and electrochemical properties. The developed process is free of cross-linker or functionalization agents and offers control over the alignment of the 2D flakes in the fabricated 3D aerogels structure.

MXenes were first discovered by Naguib et al. [15] in 2011, and since then various members of this compositionally diverse family of 2D materials have shown excellent properties for applications such as energy storage and conversion, membrane separation, sensors, electromagnetic interference shielding, and many other applications [12,16–21]. MXenes are recognized with a general formula of $M_{n+1}X_nT_x$ where 'M' is a transition metal (such as Ti, V, Cr), X is C and N, T_x represents surface functional groups (O^-, OH^-, and F^- which are randomly distributed), and *n* is an integer between 1 and 4. MXenes are synthesized by selectively etching A-layer atoms (where A is a group 13 or 14 elements such as Al, Si, Ga) from the structure of layered MAX phases with the general formula of M_nAX_{n-1}, where M, X, A, and n are the same as described above [16]. The functionalized transition metal layer at the surfaces of MXene show oxide/hydroxide like properties and are redox-active, while the metal carbide inner layers of MXene show high conductivities and facilitate electron transport to electrochemically active sites [16]. The 2D layered structure of MXenes can be intercalated with water, organic molecules, and inorganic/organic ions, which often results in increased interlayer spacings of MXenes and improved ionic transport properties [16,22].

Freeze-casting has been widely used in fabrication of freestanding 3D macroporous structures based on 2D materials such as graphene and boron nitride [23–26]. This method consists of two key steps: freezing and freeze-drying. In the freezing step, a precursor suspension, which is composed of a liquid solvent and solute particles, is frozen inside a mold to provide the desired shape. During freezing, the solute particles are rejected by growing crystals of solvent, which results in a tightly packed network of solute particles. With the applied low temperature and pressure during the freeze-drying step, solidified solvent crystals are sublimated, and a porous structure whose morphology is a replica of the solvent crystals is obtained [27,28]. Growth of the solvent crystals can be oriented with a temperature gradient, as seen in unidirectional and bidirectional freeze casting to obtain aligned micro porosities [29]. Unidirectional and bidirectional freeze casting methods have been previously used to fabricate freestanding 3D aerogels made from pristine $Ti_3C_2T_x$ [30,31]. However, so far, the focus of these studies has been on the performance of MXene aerogels for electromagnetic shielding applications. A comprehensive understanding of the relations between freeze casting conditions and the morphology of the $Ti_3C_2T_x$ aerogels and their mechanical, electrical, and electrochemical properties is missing.

$Ti_3C_2T_x$, the first discovered MXene, has been extensively studied for electrochemical energy storage applications and has shown the potential to intercalate cations of different sizes and charges [12,15,22,32–37]. Several previous studies have explored strategies to improve the performance of $Ti_3C_2T_x$ electrodes tested in batteries and electrochemical capacitors by the design and synthesis of materials and electrode structures with enhanced ionic and electronic conductivities. These include hybridization of $Ti_3C_2T_x$ with other nanomaterials such as carbon nanotubes (CNTs) [9,38] and various polymers [19,39–41], or synthesizing porous $Ti_3C_2T_x$ flakes [42]. Also, electrodes with 3D structures such as aerogel films and structures formed by crumpled MXene flakes have been fabricated, and their improved ion accessibility has been reported [43]. However, the vast majority of studies on the electrical, mechanical, and electrochemical properties of various MXenes have been limited to freestanding films or thin films deposited on a substrate [7,16,17,20,38,42,44–47].

In this article, the effect of process parameters such as freezing temperature and dispersion concentration on the microstructure of MXene aerogels and their mechanical, electrical, and electrochemical properties are reported. A unidirectional freeze casting process was employed to control the alignment of the MXene flakes in the aerogel structure. It was found that aerogels fabricated by freeze casting at −70 °C using a colloidal dispersion of $Ti_3C_2T_x$ with a concentration of 9 mg/mL can be fully recovered from 50% of compressive strain. As expected, the current–voltage curves of the fabricated aerogels showed that their electrical conductivities follow the Ohm's law. The measurements of electrical resistance under cyclic loading confirmed the excellent electro-mechanical properties of MXene aerogels and their significantly robust structures. To examine their electrochemical properties, we studied the performance of MXene aerogels as electrodes of Li-ion capacitors and found that the microstructure of aerogel electrodes has an immense impact on their specific capacity, rate capability, and cycling performance. The properties of MXene aerogels with aligned MXene flakes demonstrate their high potential for a range of applications, including energy storage devices and strain sensors.

2. Experimental

2.1. Preparation of $Ti_3C_2T_x$ colloidal dispersions

The dispersions of $Ti_3C_2T_x$ in water were prepared based on a previously reported method [48]. Briefly, concentrated hydrochloric acid (HCl, ACS Grade, BDH) solution was diluted with DI water to obtain 20 mL of 9 M HCl solution. About 1 g lithium fluoride (LiF, 98+% purity, Alfa Aesar) was added to the solution and stirred for 10 min using Teflon coated magnetic stir bars at room temperature. Then, 1 g of Ti_3AlC_2 powder was slowly added to the solution (to prevent overheating). The mixture was transferred to a hot bath and kept at 35 °C for 24 h while stirring. The mixture was then washed several times with DI water and centrifuged at 3500 rpm until the pH of the supernatant reached ~6. The MXene powder was collected, redispersed in water, and tip sonicated (Qsonica Q700) for 1 h with a power of 35 W. The resulting dispersion was centrifuged at 3500 rpm for 1 h, and the supernatant was collected and used as the base material.

2.2. Unidirectional freeze casting

The $Ti_3C_2T_x$ aerogels were prepared by a unidirectional freeze casting process. This technique generally consists of freezing the liquid dispersion on a cold plate and then freeze-drying. Three $Ti_3C_2T_x$ dispersions with concentrations of 9 mg/mL, 7 mg/mL, and 5 mg/mL were prepared. Each dispersion (1.4 mL) was poured in a cylindrical aluminum foil mold with a diameter of 15mm, placed on a cold plate, and was kept there at the desired freezing temperature for 30 min for sufficient freezing. Then, the frozen samples were transferred to a −70 °C freezer and kept there for 24 h. Repeating the same procedure, the temperature of the cold plate was adjusted to −50 °C and −30 °C to prepare the second and third batches, respectively. Finally, all the frozen samples were transferred to a −35 °C freeze-dryer connected to a running vacuum pump (0.2 Pa) to prepare the $Ti_3C_2T_x$ aerogels.

2.3. Material characterization

The microstructures of the aerogels were studied using a scanning electron microscope (SEM, HELIOS nanolab 600i, FEI). X-ray diffraction (XRD) was carried out on a Rigaku Smart Lab (Tokyo, Japan) diffractometer using Cu Kα radiation (40 kV and 44 mA) and step scan 0.02°, 3°–20° 2 theta range, and step time of 0.5 s.

Nitrogen adsorption–desorption (Quantachrome, NOVA 2000, Boynton Beach, FL, USA) was used to obtain surface area and pore size distribution via the Brunauer–Emmett–Teller (BET) method. A digital material testing device was used for performing the compression tests (Shimadzu Universal Testing Machine). All the compression tests were performed with a constant compression rate of 1 mm/min. The *V–I* plots for obtaining the electrical conductivity properties of the MXene aerogels were measured using a CHI 760D electrochemical workstation (CH Instruments, Austin, TX). The electrochemical properties of samples were tested in standard coin cells (CR-2032, MTI, Richmond, CA, USA). The $Ti_3C_2T_x$ freestanding films (punched) or $Ti_3C_2T_x$ aerogels (cut and pressed between two glass slides using a 150 g weight) were placed on copper current collectors and tested as working electrodes. The reference and counter electrodes were lithium metal foil. A polypropylene membrane (Celgard, Inc., Charlotte, NC) was used as the separator. The electrolyte was 1 M lithium hexafluorophosphate solution in ethylene carbonate and diethylcarbonate (1.0 M $LiPF_6$ in EC/DEC:50/50 (v/v)). Cyclic voltammetry (CV) was conducted at scan rates of 0.2 mV/s using a potentiostat (Biologic VMP3). The coin cells were tested in a galvanostatic mode within the voltage range of 0.01–3.01 V with respect to Li, using a battery tester (LANDT, China). Galvanostatic cycling was performed at current densities from 0.05 to 10 A/g. The mass loading of the working electrodes was 0.7–2 mg/cm^2.

3. Results and discussion

The process used for the fabrication of 3D MXene aerogels is schematically shown in Fig. 1a. MXene dispersions with known concentrations were poured into aluminum foil molds and were frozen by placing the molds on a cold plate with a precisely controlled temperature. Different freeze casting parameters, including casting temperature and dispersion concentration, were studied to find the optimal condition for $Ti_3C_2T_x$ aerogel synthesis. In unidirectional freeze casting, the temperature gradient between the cold plate and MXene dispersion is the driving force for the nucleation and directional growth of ice crystals from the bottom of the mold to its top [28]. During their growth along the temperature gradient, the ice crystals are ordered in submillimeter lamellar domains (shown in Fig. 1b and c). The MXene sheets are expelled from the freezing dispersion to the spaces between the ice crystals [49]. After the completion of the freezing step, MXene aerogels were fabricated by sublimation of the ice by a freeze-drying process, and the pores replicate the lamellar pattern of the ice. The microstructure of the aerogels fabricated through this process showed that MXene flakes are well aligned along the temperature gradient during the freezing process (Fig. 1c). The density of the fabricated MXene aerogels were in the range of 5.5 mg/cm^3 to 11.3 mg/cm^3, depending on the concentration of the dispersion used in the process. The fabricated aerogels were ultralight; they could be placed on a flower without any deformation of the plant fibers (Fig. 1d). Fig. 1e shows a transmission electron microscope (TEM) image of a representative single-layer $Ti_3C_2T_x$ flake used in the aerogel fabrication. In addition, atomic force microscopy (AFM) images and XRD patterns of synthesized $Ti_3C_2T_x$ are shown in Fig. S1 in the electronic supplementary information showing the initial solution contains MXene single flakes with an average size of 0.3 μm, and there is no new phase formation during the freeze-casting process.

The effects of fabrication conditions on the MXene aerogels microstructure were studied by comparing the top and cross-sectional SEM images of various aerogels fabricated using 5, 7, and 9 mg/mL dispersions with freezing temperatures of −30 °C, −50 °C, and −70 °C. The SEM images comparing the effects of fabrication conditions are summarized in Fig. 2. A more comprehensive presentation of SEM images of various samples can be found in Fig. S2. The top-view SEM images of aerogels, shown in Fig. 2a, c, and e, as well as Fig. S2, showed that the MXene sheets are ordered in individual domains, and cross-sectional SEM images of the microstructures shown in Fig. 2b, d, and f, confirmed the alignment of the MXene sheets along the temperature gradient (from bottom to top).

The SEM images also showed the dependence of the microstructure of aerogels on the concentration of the dispersions used in their fabrication and the freezing temperature. For a fixed concentration, the aerogels prepared at lower freezing temperatures showed a morphology that consists of submillimeter domains with well-aligned MXene sheets inside each domain, while the samples prepared at higher freezing temperatures showed less ordered structures (Fig. 2c and e). The difference in the microstructure can be related to the fact that at a lower freezing temperature, the ice crystals grow faster with smaller initial crystal nucleates, leading to the formation of thinner crystals in the MXene dispersion [50]. The thinner ice crystals also resulted in finer pores in the resulting aerogels, as shown in Fig. 2e and f, and higher surface area confirmed with BET surface area analysis (Fig. S3). The surface area based on the density functional theory method was calculated to be 162.98 m^2/g, 266.14 m^2/g, and 296.45 m^2/g for samples fabricated at −30 °C, −50 °C, and −70 °C, respectively. The SEM images showed that the aerogel fabricated using the most concentrated MXene dispersion (9 mg/mL) and lowest freezing temperature (−70 °C) has a more uniform structure with distinguishable aligned MXene walls. However, the aerogel structures showed less uniformity and alignment when the concentration of dispersion was decreased or freezing temperature was increased. The observed differences in the microstructures suggested that the aerogels fabricated using dispersions with higher concentrations and at lower freezing temperatures show better structural integrity, more aligned flakes, and finer pore structures, which can positively impact the mechanical, electrical, and electrochemical properties of the aerogels. Understanding the mechanical properties of fabricated aerogels can help to evaluate their potential for various applications, where good mechanical properties are required.

Previously, Lipatov et al. [51] investigated the elastic properties of $Ti_3C_2T_x$ mono- and bilayer sheets and reported that the effective Young's modulus of single-layer $Ti_3C_2T_x$ (0.33 TPa) is the highest among previously studied solution-processed 2D materials. Experimental characterization of the mechanical properties of MXenes has also been performed on cylindrical samples made by rolling MXene films (prepared by vacuum-assisted filtration) by Zheng et al. [7], demonstrating that a MXene film with a thickness of 5 μm can support ~4000 times its weight. The mechanical properties of MXene aerogels in this study were characterized by conducting monotonic uniaxial compression tests and measuring the compressive stress (σ) as a function of strain (ε) [52–55].

The uniaxial compression tests were performed on aerogel samples prepared at different freezing temperatures using dispersion with different concentrations, as mentioned previously. The results of in-plane compression tests of samples are summarized in Fig. 3. The stress–strain curves contain five stepped compression cycles with strain magnitudes of 10%, 20%, 30%, 40%, and 50% in sequence. The starting compression point of each cycle was the same and equaled the original height of the sample [56]. Interestingly, the stress–strain curves show that some of the fabricated aerogels can withstand almost 50% of strain and then recover to their original shape, demonstrating that for some processing conditions, the $Ti_3C_2T_x$ aerogels have a good compression capability and strain memory effect.

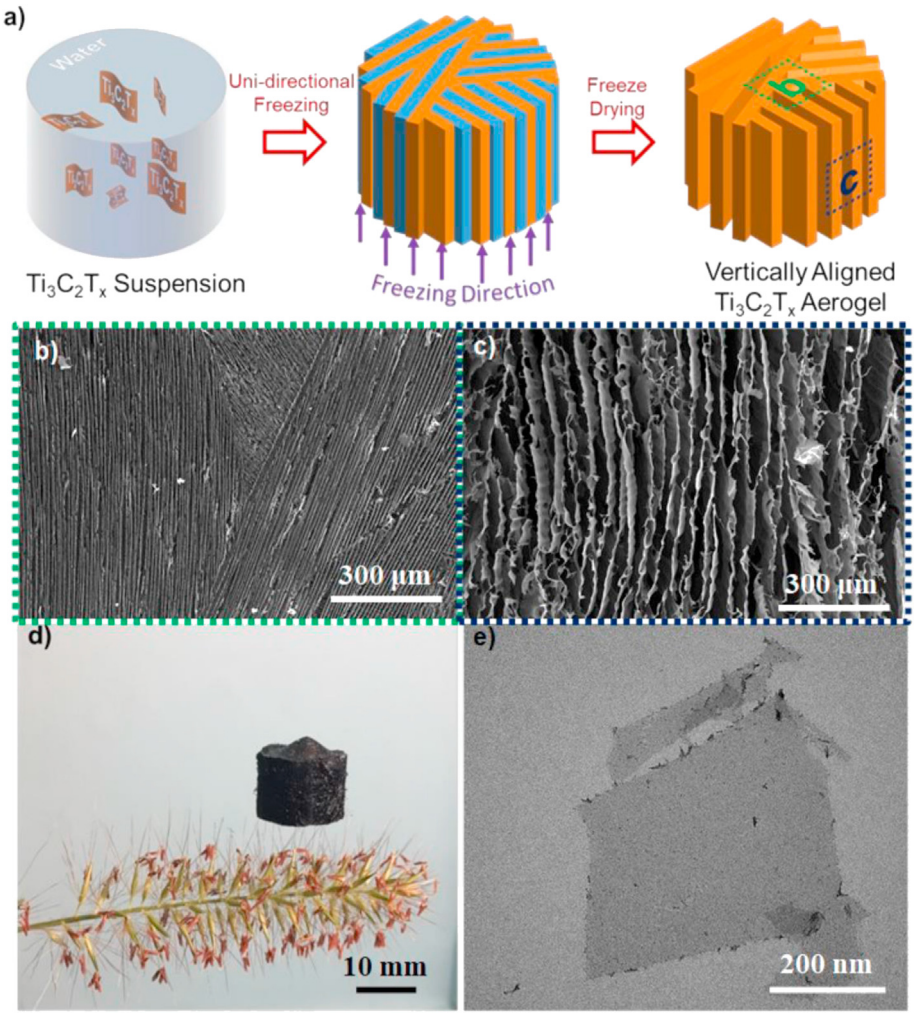

Fig. 1. (a) Schematic demonstration of the aerogel fabrication process. (b–c) Top view and cross-sectional view SEM image of MXene aerogels. (d) An ultralight $Ti_3C_2T_x$ aerogel placed on a flower. (e) TEM image of a single-layer $Ti_3C_2T_x$ flake.

Reducing the freezing temperature at fixed dispersion concentration significantly enhanced the structural integrity (Fig. 3a and b). Regardless of the freezing temperature, the aerogels prepared using a dispersion of lower concentrations of MXene did not show a good response to the compression force (Fig. S4). Aerogels prepared using dispersions with a higher concentration (9 mg/mL) demonstrated a higher compressive stress tolerance and better structural integrity for all freeze casting temperatures (Fig. 3c and d). For the same dispersion concentration, the aerogels fabricated at lower temperatures showed higher compressive strengths. The samples prepared using a dispersion concentration of 9 mg/mL and freeze casting temperature of −70 °C demonstrated the highest compressive strength and the highest compression recovery capability under 50% of compression (Fig. 3d). The loading curves in Fig. 3d show the three distinct regions that are typically observed in mechanical testing of cellular materials, namely the initial Hookean region at $5\% < \varepsilon < 10\%$, plateau region at $12\% < \varepsilon < 26\%$, and densification region for $\varepsilon > 30\%$ with a sharp increase in stress [52,56]. The initial increase of stress for $\varepsilon < 5\%$ is caused by the increase in the contact area between the sample and compression plate [56].

The observed hysteresis loops in the loading–unloading curves indicate the high energy dissipation capability of all the fabricated aerogels [56,57]. The energy dissipation can be attributed to the buckling of 2D $Ti_3C_2T_x$ sheets, the adhesion forces between sheets that cause friction between them, and the formation of cracks under large compressive strains [56]. The linear elastic bending mode deformation of MXene sheets is primarily responsible for the Hookean region [56]. The plateau region that follows the Hookean region is primarily governed by the buckling deformation of MXene sheets [56].

To further determine the stability of the aerogels under cyclic loading, compression up to 10% strain was applied for 100 cycles (Fig. 3e). The second loading–unloading curve exhibits a 5.2% degradation of stress achieved in the first cycle, meaning that the $Ti_3C_2T_x$ aerogels maintain their original elasticity and structural robustness. It is worth noting that MXene aerogels have similar compression modulus values compared to other reported aerogels with similar relative densities (Fig. 3f) [58–61]. Overall, all the specimens demonstrated high compressive recovery capability, presenting unidirectional freeze casting as a feasible and reliable methodology to fabricate freestanding MXene aerogels for possible structural applications.

We further investigated the effect of MXene dispersion concentration and the freezing temperature on the electrical and electrochemical properties of the fabricated aerogel. Fig. 4a shows the current-voltage (I–V) curves of samples with different densities ranging from 5.5 to 11.3 mg/cm^3. The insert picture in Fig. 4a shows

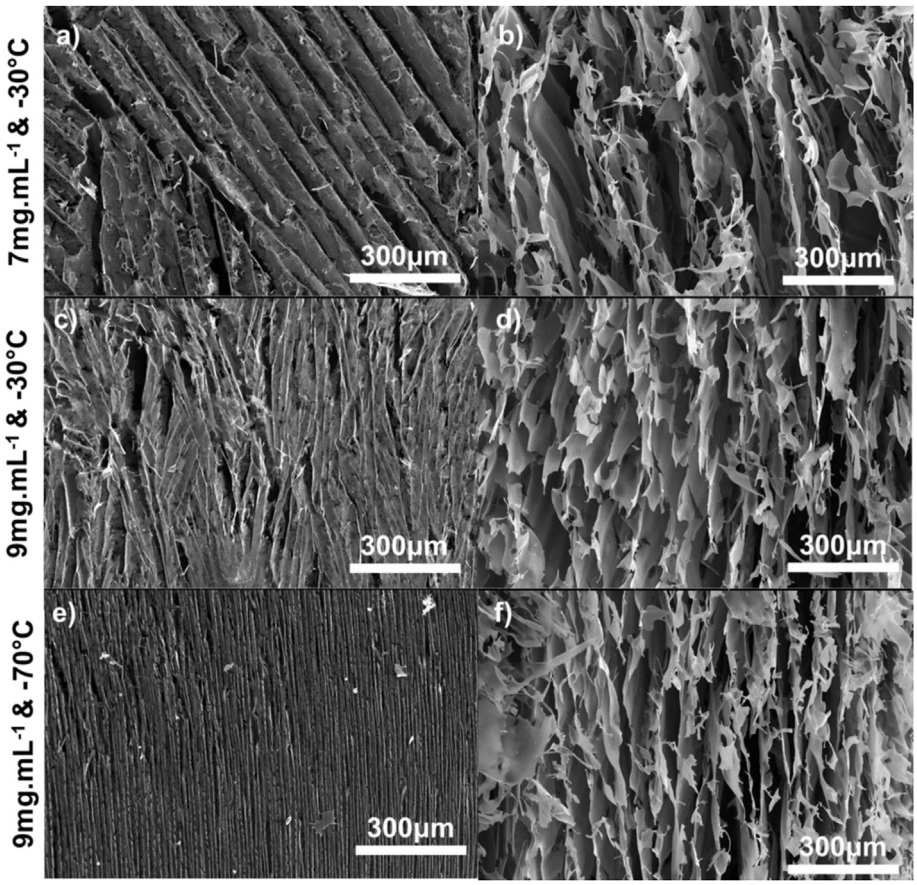

Fig. 2. SEM images of the $Ti_3C_2T_x$ aerogels fabricated with different conditions. Top surface and cross sectional view of the $Ti_3C_2T_x$ aerogels prepared using (a–b) 7 mg/mL dispersion with a freezing temperature of −30 °C, (c–d) 9 mg/mL dispersion with a freezing temperature of −30 °C, and (e–f) 9 mg/mL dispersion with a freezing temperature of −70 °C.

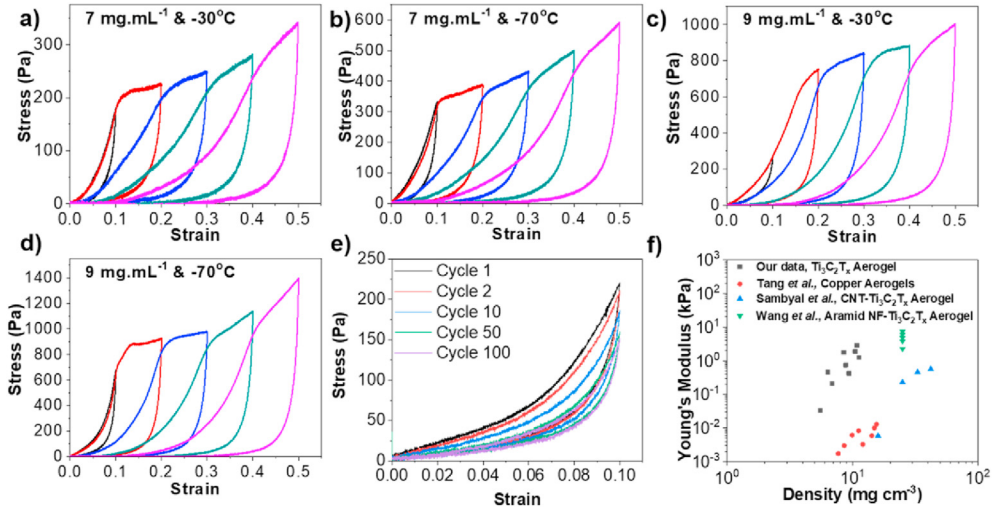

Fig. 3. (a–d) Stress–strain curves during loading–unloading cycles by increasing strain amplitude for MXene aerogels fabricated using 7 mg/mL and 9 mg/mL dispersions with freezing temperatures of −30 °C and −70 °C. (e) The stress–strain curves for cyclic loading-unloading compression tests of a $Ti_3C_2T_x$ aerogel fabricated from 9 mg/mL dispersion with a freezing temperature of −50 °C. (f) Compression modulus vs. density of the fabricated aerogels and similar aerogels reported in the literature.

a demonstration of the high electrical conductivity of a MXene aerogel. The current responses of all aerogels followed Ohm's law, presenting a typical linear relationship with applied voltage [52,54]. For the same freezing temperature, an aerogel prepared using a dispersion with a higher concentration than 7 mg/mL demonstrates a higher current under the same applied voltage, which means it has a lower electrical resistance. Interestingly, the aerogels prepared at the freezing temperature of −50 °C show the

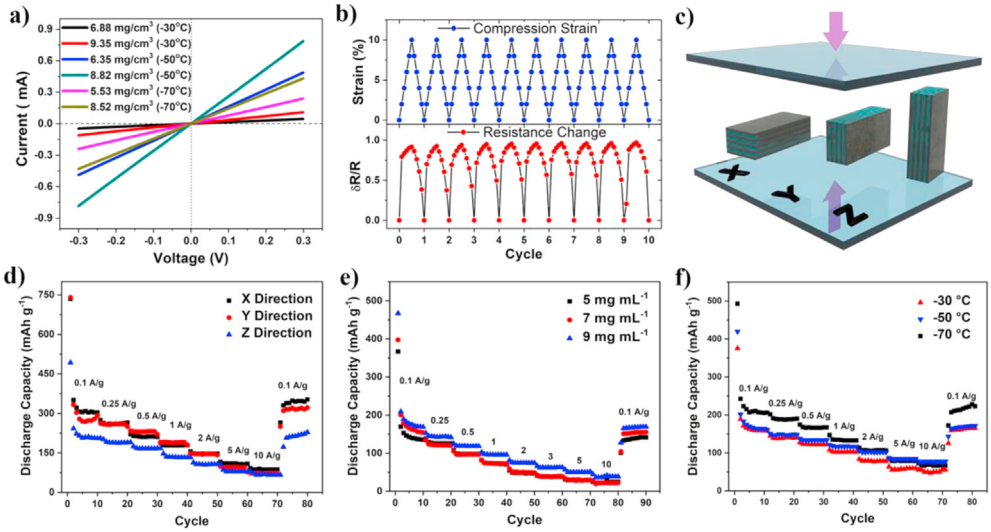

Fig. 4. Electrical and electrochemical properties of MXene aerogels fabricated at different conditions. (a) I–V curves of MXene aerogels. The insert shows the electrical conductivity of MXene aerogels. (b) Resistivity change against compressive cycles. (c) Pressing directions are defined based on the direction of the domains. (d, e, f) Electrochemical performance of MXene aerogels based on pressing direction (9 mg/mL dispersion freeze casted at −70 °C), dispersion concentration (freeze-casted at −30 °C), and freezing temperature (7 mg/mL dispersion).

lowest electrical resistance. We believe that the higher density and the thicker MXene walls obtained for sample freeze-casted at −50 °C may have resulted in a higher conductivity of these samples [62]. The samples produced at −30 °C, −50 °C, and −70 °C freezing temperatures with 7 mg/mL dispersion concentration showed electrical resistances of ~49.27 × 10^3 Ω mm, ~6.05 × 10^3 Ω mm, and ~12.53 × 10^3 Ω mm, respectively. The measured data suggests that electrical resistance increases rapidly as the density decreases as a result of the increased porosity and less intersheet junctions in the aerogels with lower densities [54]. As shown in Fig. 4b, the electrical resistance of the freeze-casted MXene aerogel is highly consistent over multiple compression cycles (10 cycles are shown in Fig. 4b), indicating the significant structural resilience of aerogels under cyclic loading [57].

The freeze-dried aerogels showed different domains and directions in their microstructures (Fig. 1). Thus, the freeze casted samples were tested as electrode material for Li-ion storage in various directions (the aerogel was pressed between two glass slides before assembling a coin cell, as shown in Fig. 4c). The electrochemical studies indicated that pressing in the X direction (Fig. 4c and d) with minimum change in dimensions delivered the best electrochemical response compared with the other pressing directions, probably due to the minimal structural damage. The $Ti_3C_2T_x$ aerogel electrode delivered the initial discharge and charge capacities of 755 and 435 mAh/g, respectively. The irreversible capacity loss in the first cycle is primarily attributed to the solid electrolyte interphase formation, electrolyte decomposition, or irreversible reactions of various surface functional groups (O^-, OH^-, and F^-) [63–67].

The as-fabricated $Ti_3C_2T_x$ aerogel electrodes showed a gravimetric capacity of ~330 mAh/g at a 0.1 A/g current density (Fig. 4d). However, as explained below, the specific capacity of the MXene aerogels significantly increased after their continuous cycling. Nevertheless, the as-fabricated aerogel electrodes showed higher specific capacities compared to previously reported freestanding $Ti_3C_2T_x$ films [12]. They also exhibited a good rate capability due to their open pore structures, which facilitates electrolyte transport while preserving their high electrical conductivity. Specific capacities of up to ~100 mAh/g and ~75 mAh/g were obtained at high rates of 5 A/g and 10 A/g, respectively. During the cyclic tests, for all samples, the coulombic efficiency rapidly reached ~100% after the second cycle and was constant during the remaining cycles. The electrochemical tests suggest that aerogels fabricated using dispersions with higher concentrations and at lower freeze casting temperature showed a better electrochemical response in terms of specific capacity and rate handling capability (Fig. 4e and f). This could be related to the increased interlayer spacing of aerogels fabricated at lower freeze-casting temperatures. As shown in Fig. S5, the corresponding (0002) plane of MXene downshifts from 6.69° to 6.06° for the MXene film and freeze-casted aerogel at −70 °C, respectively. This corresponds to a 1.4 Å larger d-spacing for the freeze-casted aerogel. It is worth mentioning that at high current densities, the aerogels freeze casted at −50 °C showed better electrochemical performance, which is in line with the higher electrical conductivity of these samples.

The cyclic tests of the aerogel electrodes showed that their capacities gradually increased during the first few hundred cycles. Fig. 5a shows the cyclic performance of a MXene aerogel electrode (fabricated using a 9 mg/mL dispersion with a freeze casting temperature of −70 °C) tested at a constant charge/discharge current density of 0.5 A/g. The specific capacity of the electrode dropped in the first ~15 cycles (stabilization) and then continuously increased over the next ~900 cycles followed by a steady performance for the remaining cycles. This continuous increase in capacity suggests that the accessibility of Li ions to the active sites between MXene layers improves over cycling due to the minimize restacking of the MXene flakes [39,43]. The as-fabricated aerogels have porous structures, and the walls consist of several MXene layers. The interlayer spacing of these layers is not readily accessible to Li ions. During each cycle, the intercalation of Li ions, which may be completely or partially dissolved, increases the interlayer spacing and more ions can intercalate between the layers in the subsequent cycles. Therefore, the specific capacity of the aerogel electrodes continuously increases until the maximum expansion in the interlayer spacing is achieved. The porous structure of aerogels allows the expansion of the interlayer spacing while preserving the structure of the electrodes and electrical connectivity of MXene flakes. Also, the ordering of the flakes in the structure facilitates the uniform expansion of their interlayer spacing. Therefore, we believe that the porous structure of the as-fabricated aerogels has an immense

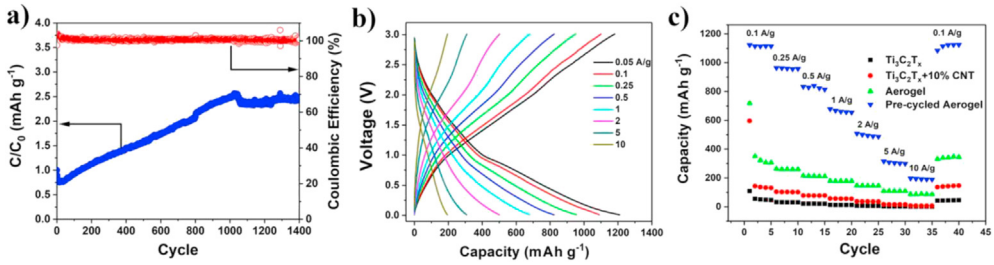

Fig. 5. Li ion storage performance of $Ti_3C_2T_x$ aerogels electrodes. (a) Capacity retention, cycling stability, and Coulombic efficiency of $Ti_3C_2T_x$ aerogel electrodes test at a current density of 0.5 A/g. (b) Voltage profiles of precycled aerogel at various current densities (A/g); (c) Discharge capacities at different current densities for $Ti_3C_2T_x$ aerogels, films and $Ti_3C_2T_x$-CNT composite film.

impact on this electrochemical activation phenomenon (i. e., the improved performance of the electrodes during each cycle). As shown in Fig. S6, when a freestanding MXene electrode fabricated by vacuum-assisted filtration was tested under the same conditions, it showed much lower initial capacity (14 mAh/g at 0.5 A/g) with a slight increase of capacity over cycling.

The cycled aerogel electrodes were tested at different current densities to understand the effects of the electrochemical activation on the performance of the electrodes (Fig. 5a and Fig. S7). The CV test result of the first few cycles showed a pseudo-rectangular shape with very broad lithiation and de-lithiation peaks, representing the capacitive performance of the electrodes (Fig. S7), which is in line with previous reports of the MXene electrodes for Li-ion capacitors. The CV tests were also performed on electrodes after 700 charge-discharge cycles at 0.5 A/g and showed a similar pseudo-rectangular shape with the substantially increased area due to the improved capacity of the electrodes after cycling (Fig. S7). Therefore, the CV and voltage profiles of the aerogel electrodes showed that they are excellent electrodes for Li-ion capacitors.

The cycled electrodes (cycled for a few hundred cycles) were tested at various current rates, which showed their excellent cyclability and rate handling capability. A high specific capacity of ~1210 mAh/g was achieved at 0.05 A/g, which gradually decreases to ~200 mAh/g at a very high current density of 10 A/g (Fig. 5b and c). As explained above, we attribute the significant improvement in the electrochemical performance of the electrodes to the improved ionic transport properties of the aerogels due to the increase in the interlayer spacing. It is worth noting that the measured specific capacities of the cycled electrode at all current densities significantly exceed those previously reported for MXene Li-ion capacitors tested at the same current densities [12]. The performance of the MXene aerogel electrodes was compared with two of the most commonly tested electrode structures for MXenes, freestanding films of MXene or MXene/CNT hybrids, fabricated by vacuum-assisted filtration. As shown in Fig. 5c, the cycled aerogel electrodes showed significantly higher specific capacities compared to these electrodes at all tested current densities.

4. Conclusion

In summary, freestanding, binder and additive-free, and ultralight weight (density below 11.3 mg/cm^3) MXene aerogels with ordered structures were fabricated through unidirectional freeze casting. It was demonstrated that the processing conditions, such as freezing temperature and dispersion concentration, can control the structural, mechanical, electrical, and electrochemical properties of fabricated aerogels. Our studies of the morphology of MXene aerogels showed the alignment of MXene flakes in submillimeter domains along the temperature gradient. The compression tests showed that MXene aerogels could withstand and recover from compressive strains up to 50%. The MXene aerogels showed superior electrochemical response with excellent cyclic stability, high specific capacity, and excellent rate performance. The electrochemical studies of the aerogels, as electrodes for Li-ion capacitors, showed that the capacity of the electrodes gradually increases during the cycling. After activation with cycling, the MXene aerogel electrode showed outstanding performance, surpassing the performance of previously reported $Ti_3C_2T_x$ electrodes tested as electrodes for Li-ion capacitors. We believe that employing strategies to prevent restacking of the MXene flakes during aerogel fabrication would eliminate the need for electrochemical cycling to achieve maximum capacity. Also, we believe that the electrical and mechanical properties of the MXene aerogels make them a promising candidate for a range of other applications. For example, the excellent electro-mechanical properties of MXene aerogels under cyclic loading can be exploited to fabricate high-performance strain sensors.

Author's contribution

Jafar Orangi: Methodology, Validation, Formal Analysis, Investigation, Writing – Original Draft, Visualization.

Halil Tetik: Methodology, Validation, Formal Analysis, Investigation, Writing – Original Draft, Visualization.

Pedram Parandoush: Methodology, Investigation.

Emre Kayali: Methodology, Investigation.

Dong Lin: Conceptualization, Methodology, Resources, Writing – Review and Editing, Supervision, Project Administration, Funding Acquisition.

Majid Beidaghi: Conceptualization, Methodology, Resources, Writing – Review and Editing, Supervision, Project Administration, Funding Acquisition.

Declaration of competing interest

The authors declare that they have no known competing financial interests or personal relationships that could have appeared to influence the work reported in this article.

Acknowledgments

J. O. and H. T. equally contributed to this work. This work was partly supported by the National Science Foundation grant (OAI-1929195). J. O. acknowledges the support from the Alabama EPSCoR Graduate Research Scholar Program (GRSP Round 12-14) doctoral fellowship. D. L. thanks the support from the National Science Foundation under Award No. 1943445, NASA EPSCoR Cooperative Agreement Notice award number 80NSSC19M0153, and the support from Johnson Cancer Center. HT acknowledges the graduate

research scholarship from the Turkish Ministry of National Education.

Appendix B. Supplementary data

Supplementary data to this article can be found online at https://doi.org/10.1016/j.mtadv.2021.100135.

References

[1] X. Cao, Z. Yin, H. Zhang, Three-dimensional graphene materials: preparation, structures and application in supercapacitors, Energy Environ. Sci. 7 (2014) 1850–1865.

[2] Q. Fang, Y. Shen, B. Chen, Synthesis, decoration and properties of three-dimensional graphene-based macrostructures: a review, Chem. Eng. J. 264 (2015) 753–771.

[3] E. García-Tuñon, S. Barg, J. Franco, R. Bell, S. Eslava, E. D'Elia, R.C. Maher, F. Guitian, E. Saiz, Printing in three dimensions with graphene, Adv. Mater. 27 (2015) 1688–1693.

[4] J. Zhu, E. Ha, G. Zhao, Y. Zhou, D. Huang, G. Yue, L. Hu, N. Sun, Y. Wang, L.Y.S. Lee, Recent advance in MXenes: a promising 2D material for catalysis, sensor and chemical adsorption, Coord. Chem. Rev. 352 (2017) 306–327.

[5] H. An, T. Habib, S. Shah, H. Gao, M. Radovic, M.J. Green, J.L. Lutkenhaus, Surface-agnostic highly stretchable and bendable conductive MXene multilayers, Sci. Adv. 4 (2018), eaaq0118.

[6] Y. Cai, J. Shen, G. Ge, Y. Zhang, W. Jin, W. Huang, J. Shao, J. Yang, X. Dong, Stretchable $Ti_3C_2T_x$ MXene/carbon nanotube composite based strain sensor with ultrahigh sensitivity and tunable sensing range, ACS Nano 12 (2017) 56–62.

[7] Z. Ling, C.E. Ren, M.-Q. Zhao, J. Yang, J.M. Giammarco, J. Qiu, M.W. Barsoum, Y. Gogotsi, Flexible and conductive MXene films and nanocomposites with high capacitance, Proc. Natl. Acad. Sci. Unit. States Am. 111 (2014) 16676–16681.

[8] Y. Dall'Agnese, M.R. Lukatskaya, K.M. Cook, P.-L. Taberna, Y. Gogotsi, P. Simon, High capacitance of surface-modified 2D titanium carbide in acidic electrolyte, Electrochem. Commun. 48 (2014) 118–122.

[9] M.-Q. Zhao, C.E. Ren, Z. Ling, M.R. Lukatskaya, C. Zhang, K.L. Van Aken, M.W. Barsoum, Y. Gogotsi, Flexible MXene/carbon nanotube composite paper with high volumetric capacitance, Adv. Mater. 27 (2015) 339–345.

[10] Q. Hu, D. Sun, Q. Wu, H. Wang, L. Wang, B. Liu, A. Zhou, J. He, MXene: a new family of promising hydrogen storage medium, J. Phys. Chem. 117 (2013) 14253–14260.

[11] T. Zhang, L. Pan, H. Tang, F. Du, Y. Guo, T. Qiu, J. Yang, Synthesis of two-dimensional $Ti_3C_2T_x$ MXene using HCl+ LiF etchant: enhanced exfoliation and delamination, J. Alloys Compd. 695 (2017) 818–826.

[12] J. Orangi, M. Beidaghi, A review of the effects of electrode fabrication and assembly processes on the structure and electrochemical performance of 2D MXenes, Adv. Funct. Mater. (2020) 2005305.

[13] J. Jiang, Y. Li, J. Liu, X. Huang, C. Yuan, X.W. Lou, Recent advances in metal oxide-based electrode architecture design for electrochemical energy storage, Adv. Mater. 24 (2012) 5166–5180.

[14] S.M. Jung, D.L. Mafra, C.-T. Lin, H.Y. Jung, J. Kong, Controlled porous structures of graphene aerogels and their effect on supercapacitor performance, Nanoscale 7 (2015) 4386–4393.

[15] M. Naguib, M. Kurtoglu, V. Presser, J. Lu, J. Niu, M. Heon, L. Hultman, Y. Gogotsi, M.W. Barsoum, Two-dimensional nanocrystals produced by exfoliation of Ti_3AlC_2, Adv. Mater. 23 (2011) 4248–4253.

[16] B. Anasori, M.R. Lukatskaya, Y. Gogotsi, 2D metal carbides and nitrides (MXenes) for energy storage, Nat. Rev. Mater. 2 (2017) 16098.

[17] E. Kayali, A. VahidMohammadi, J. Orangi, M. Beidaghi, Controlling the dimensions of 2D MXenes for ultra-high-rate pseudocapacitive energy storage, ACS Appl. Mater. Interfaces 10 (2018) 25949–25954.

[18] E. Lee, A. VahidMohammadi, B.C. Prorok, Y.S. Yoon, M. Beidaghi, D.-J. Kim, Room temperature gas sensing of two-dimensional titanium carbide (MXene), ACS Appl. Mater. Interfaces 9 (2017) 37184–37190.

[19] A. VahidMohammadi, J. Moncada, H. Chen, E. Kayali, J. Orangi, C.A. Carrero, M. Beidaghi, Thick and freestanding MXene/PANI pseudocapacitive electrodes with ultrahigh specific capacitance, J. Mater. Chem. A. 6 (2018) 22123–22133.

[20] N. Shpigel, M.D. Levi, S. Sigalov, T.S. Mathis, Y. Gogotsi, D. Aurbach, Direct assessment of nano-confined water in 2D Ti_3C_2 (MXene) electrode interspaces by a surface acoustic technique, J. Am. Chem. Soc. 140 (28) (2018) 8910–8917.

[21] J. Orangi, F. Hamade, V.A. Davis, M. Beidaghi, 3D printing of additive-free 2D $Ti_3C_2T_x$ (MXene) ink for fabrication of micro-supercapacitors with ultra-high energy densities, ACS Nano 14 (2019) 640–650.

[22] P. Lian, Y. Dong, Z.-S. Wu, S. Zheng, X. Wang, S. Wang, C. Sun, J. Qin, X. Shi, X. Bao, Alkalized Ti_3C_2 MXene nanoribbons with expanded interlayer spacing for high-capacity sodium and potassium ion batteries, Nanomater. Energy 40 (2017) 1–8.

[23] J. Wang, D. Liu, Q. Li, C. Chen, Z. Chen, P. Song, J. Hao, Y. Li, S. Fakhrhoseini, M. Naebe, Lightweight, superelastic yet thermoconductive boron nitride nanocomposite aerogel for thermal energy regulation, ACS Nano 13 (2019) 7860–7870.

[24] X. Zeng, L. Ye, S. Yu, R. Sun, J. Xu, C.-P. Wong, Facile preparation of superelastic and ultralow dielectric boron nitride nanosheet aerogels via freeze-casting process, Chem. Mater. 27 (2015) 5849–5855.

[25] W. Gao, N. Zhao, W. Yao, Z. Xu, H. Bai, C. Gao, Effect of flake size on the mechanical properties of graphene aerogels prepared by freeze casting, RSC Adv. 7 (2017) 33600–33605.

[26] C. Wang, X. Chen, B. Wang, M. Huang, B. Wang, Y. Jiang, R.S. Ruoff, Freeze-casting produces a graphene oxide aerogel with a radial and centrosymmetric structure, ACS Nano 12 (2018) 5816–5825.

[27] M. Naviroj, S.M. Miller, P. Colombo, K.T. Faber, Directionally aligned macroporous SiOC via freeze casting of preceramic polymers, J. Eur. Ceram. Soc. 35 (2015) 2225–2232.

[28] S. Deville, Freeze-casting of porous ceramics: a review of current achievements and issues, Adv. Eng. Mater. 10 (2008) 155–169.

[29] K.L. Scotti, D.C. Dunand, Freeze casting–A review of processing, microstructure and properties via the open data repository, in: FreezeCasting. net, Prog. Mater. Sci., vol. 94, 2018, pp. 243–305.

[30] R. Bian, G. He, W. Zhi, S. Xiang, T. Wang, D. Cai, Ultralight MXene-based aerogels with high electromagnetic interference shielding performance, J. Mater. Chem. C. 7 (2019) 474–478.

[31] M. Han, X. Yin, K. Hantanasirisakul, X. Li, A. Iqbal, C.B. Hatter, B. Anasori, C.M. Koo, T. Torita, Y. Soda, Anisotropic MXene aerogels with a mechanically tunable ratio of electromagnetic wave reflection to absorption, Adv. Opt. Mater. 7 (2019) 1900267.

[32] M. Naguib, J. Halim, J. Lu, K.M. Cook, L. Hultman, Y. Gogotsi, M.W. Barsoum, New two-dimensional niobium and vanadium carbides as promising materials for Li-ion batteries, J. Am. Chem. Soc. 135 (2013) 15966–15969, https://doi.org/10.1021/ja405735d.

[33] M. Naguib, O. Mashtalir, J. Carle, V. Presser, J. Lu, L. Hultman, Y. Gogotsi, M.W. Barsoum, Two-dimensional transition metal carbides, ACS Nano 6 (2012) 1322–1331.

[34] M. Naguib, Y. Gogotsi, Synthesis of two-dimensional materials by selective extraction, Acc. Chem. Res. 48 (2015) 128–135, https://doi.org/10.1021/ar500346b.

[35] I. Demiroglu, F.M. Peeters, O. Gülseren, D. Çakır, C. Sevik, Alkali metal intercalation in MXene/graphene heterostructures: a new platform for ion battery applications, J. Phys. Chem. Lett. 10 (2019) 727–734, https://doi.org/10.1021/acs.jpclett.8b03056.

[36] M.R. Lukatskaya, O. Mashtalir, C.E. Ren, Y. Dall'Agnese, P. Rozier, P.L. Taberna, M. Naguib, P. Simon, M.W. Barsoum, Y. Gogotsi, Cation intercalation and high volumetric capacitance of two-dimensional titanium carbide, Science 341 (2013) 1502–1505.

[37] M. Boota, M. Pasini, F. Galeotti, W. Porzio, M.-Q. Zhao, J. Halim, Y. Gogotsi, Interaction of polar and nonpolar polyfluorenes with layers of two-dimensional titanium carbide (MXene): intercalation and pseudocapacitance, Chem. Mater. 29 (2017) 2731–2738, https://doi.org/10.1021/acs.chemmater.6b03933.

[38] Y. Dall'Agnese, P. Rozier, P.-L. Taberna, Y. Gogotsi, P. Simon, Capacitance of two-dimensional titanium carbide (MXene) and MXene/carbon nanotube composites in organic electrolytes, J. Power Sources 306 (2016) 510–515.

[39] W. Tian, A. VahidMohammadi, Z. Wang, L. Ouyang, M. Beidaghi, M.M. Hamedi, Layer-by-layer self-assembly of pillared two-dimensional multilayers, Nat. Commun. 10 (2019) 2558, https://doi.org/10.1038/s41467-019-10631-0.

[40] M. Boota, B. Anasori, C. Voigt, M.-Q. Zhao, M.W. Barsoum, Y. Gogotsi, Pseudocapacitive electrodes produced by oxidant-free polymerization of pyrrole between the layers of 2D titanium carbide (MXene), Adv. Mater. 28 (2016) 1517–1522.

[41] R. Liu, M. Miao, Y. Li, J. Zhang, S. Cao, X. Feng, Ultrathin biomimetic polymeric $Ti_3C_2T_x$ MXene composite films for electromagnetic interference shielding, ACS Appl. Mater. Interfaces 10 (2018) 44787–44795, https://doi.org/10.1021/acsami.8b18347.

[42] C.E. Ren, M.-Q. Zhao, T. Makaryan, J. Halim, M. Boota, S. Kota, B. Anasori, M.W. Barsoum, Y. Gogotsi, Porous two-dimensional transition metal carbide (MXene) flakes for high-performance Li-ion storage, ChemElectroChem 3 (2016) 689–693.

[43] M.R. Lukatskaya, S. Kota, Z. Lin, M.-Q. Zhao, N. Shpigel, M.D. Levi, J. Halim, P.-L. Taberna, M.W. Barsoum, P. Simon, Ultra-high-rate pseudocapacitive energy storage in two-dimensional transition metal carbides, Nat. Energy 2 (2017) 17105.

[44] Y. Wen, T.E. Rufford, X. Chen, N. Li, M. Lyu, L. Dai, L. Wang, Nitrogen-doped $Ti_3C_2T_x$ MXene electrodes for high-performance supercapacitors, Nanomater. Energy 38 (2017) 368–376.

[45] O. Mashtalir, K.M. Cook, V.N. Mochalin, M. Crowe, M.W. Barsoum, Y. Gogotsi, Dye adsorption and decomposition on two-dimensional titanium carbide in aqueous media, J. Mater. Chem. A. 2 (2014) 14334–14338.

[46] S.A. Shah, T. Habib, H. Gao, P. Gao, W. Sun, M.J. Green, M. Radovic, Template-free 3D titanium carbide ($Ti_3C_2T_x$) MXene particles crumpled by capillary forces, Chem. Commun. 53 (2017) 400–403.

[47] A. VahidMohammadi, A. Hadjikhani, S. Shahbazmohamadi, M. Beidaghi, Two-dimensional vanadium carbide (MXene) as a high-capacity cathode material for rechargeable aluminum batteries, ACS Nano 11 (2017) 11135–11144.

[48] M. Ghidiu, M.R. Lukatskaya, M.-Q. Zhao, Y. Gogotsi, M.W. Barsoum, Conductive two-dimensional titanium carbide 'clay'with high volumetric capacitance, Nature 516 (2014) 78.

[49] H. Bai, Y. Chen, B. Delattre, A.P. Tomsia, R.O. Ritchie, Bioinspired large-scale aligned porous materials assembled with dual temperature gradients, Sci. Adv. 1 (2015), e1500849.
[50] H.-L. Gao, L. Xu, F. Long, Z. Pan, Y.-X. Du, Y. Lu, J. Ge, S.-H. Yu, Macroscopic free-standing hierarchical 3D architectures assembled from silver nanowires by ice templating, Angew. Chem. Int. Ed. 53 (2014) 4561–4566.
[51] A. Lipatov, H. Lu, M. Alhabeb, B. Anasori, A. Gruverman, Y. Gogotsi, A. Sinitskii, Elastic properties of 2D $Ti_3C_2T_x$ MXene monolayers and bilayers, Sci. Adv. 4 (2018), eaat0491.
[52] Q. Zhang, F. Zhang, S.P. Medarametla, H. Li, C. Zhou, D. Lin, 3D printing of graphene aerogels, Small 12 (2016) 1702–1708.
[53] Q. Zhang, D. Lin, B. Deng, X. Xu, Q. Nian, S. Jin, K.D. Leedy, H. Li, G.J. Cheng, Flyweight, superelastic, electrically conductive, and flame-retardant 3D multi-nanolayer graphene/ceramic metamaterial, Adv. Mater. 29 (2017).
[54] P. Yan, E. Brown, Q. Su, J. Li, J. Wang, C. Xu, C. Zhou, D. Lin, 3D printing hierarchical silver nanowire aerogel with highly compressive resilience and tensile elongation through tunable Poisson's ratio, Small 13 (2017).
[55] Q. Zhang, X. Xu, D. Lin, W. Chen, G. Xiong, Y. Yu, T.S. Fisher, H. Li, Hyperbolically patterned 3D graphene metamaterial with negative Poisson's ratio and superelasticity, Adv. Mater. 28 (2016) 2229–2237.
[56] C. Zhu, T.Y.-J. Han, E.B. Duoss, A.M. Golobic, J.D. Kuntz, C.M. Spadaccini, M.A. Worsley, Highly compressible 3D periodic graphene aerogel microlattices, Nat. Commun. 6 (2015) 6962.
[57] L. Qiu, J.Z. Liu, S.L. Chang, Y. Wu, D. Li, Biomimetic superelastic graphene-based cellular monoliths, Nat. Commun. 3 (2012) 1241.
[58] F. Qian, P.C. Lan, M.C. Freyman, W. Chen, T. Kou, T.Y. Olson, C. Zhu, M.A. Worsley, E.B. Duoss, C.M. Spadaccini, Ultralight conductive silver nanowire aerogels, Nano Lett. 17 (2017) 7171–7176.
[59] Y. Tang, K.L. Yeo, Y. Chen, L.W. Yap, W. Xiong, W. Cheng, Ultralow-density copper nanowire aerogel monoliths with tunable mechanical and electrical properties, J. Mater. Chem. A. 1 (2013) 6723–6726.
[60] L. Wang, M. Zhang, B. Yang, J. Tan, X. Ding, Highly compressible, thermally stable, light-weight, and robust aramid nanofibers/Ti_3AlC_2 MXene composite aerogel for sensitive pressure sensor, ACS Nano 14 (2020) 10633–10647.
[61] P. Sambyal, A. Iqbal, J. Hong, H. Kim, M.-K. Kim, S.M. Hong, M. Han, Y. Gogotsi, C.M. Koo, Ultralight and mechanically robust $Ti_3C_2T_x$ hybrid aerogel reinforced by carbon nanotubes for electromagnetic interference shielding, ACS Appl. Mater. Interfaces 11 (2019) 38046–38054.
[62] C. Huang, J. Peng, S. Wan, Y. Du, S. Dou, H.D. Wagner, A.P. Tomsia, L. Jiang, Q. Cheng, Ultra-tough inverse artificial nacre based on epoxy-graphene by freeze-casting, Angew. Chem. Int. Ed. 58 (2019) 7636–7640.
[63] Y. Xie, M. Naguib, V.N. Mochalin, M.W. Barsoum, Y. Gogotsi, X. Yu, K.-W. Nam, X.-Q. Yang, A.I. Kolesnikov, P.R. Kent, Role of surface structure on Li-ion energy storage capacity of two-dimensional transition-metal carbides, J. Am. Chem. Soc. 136 (2014) 6385–6394.
[64] X. Hui, R. Zhao, P. Zhang, C. Li, C. Wang, L. Yin, Low-temperature reduction strategy synthesized Si/Ti_3C_2 MXene composite anodes for high-performance Li-ion batteries, Adv. Energy Mater. 9 (2019) 1901065.
[65] P. Yu, G. Cao, S. Yi, X. Zhang, C. Li, X. Sun, K. Wang, Y. Ma, Binder-free 2D titanium carbide (MXene)/carbon nanotube composites for high-performance lithium-ion capacitors, Nanoscale 10 (2018) 5906–5913, https://doi.org/10.1039/C8NR00380G.
[66] S. Zhao, X. Meng, K. Zhu, F. Du, G. Chen, Y. Wei, Y. Gogotsi, Y. Gao, Li-ion uptake and increase in interlayer spacing of Nb4C3 MXene, Energy Storage Mater. 8 (2017) 42–48.
[67] Y. Liu, W. Wang, Y. Ying, Y. Wang, X. Peng, Binder-free layered Ti_3C_2/CNTs nanocomposite anodes with enhanced capacity and long-cycle life for lithium-ion batteries, Dalton Trans. 44 (2015) 7123–7126.